The interplay of dissolution, solution crystallization and solid-state transformation of amorphous indomethacin in aqueous solution

Raj Schneider [a], Jana Kerkhoff [a], Andreas Danzer [a], Amelie Mattusch [b], Andrijan Ohmann [a], Markus Thommes [b], Gabriele Sadowski [a,*]

[a] TU Dortmund, Department of Biochemical and Chemical Engineering, Laboratory of Thermodynamics, Emil-Figge-Str. 70, D-44227 Dortmund, Germany
[b] TU Dortmund, Department of Biochemical and Chemical Engineering, Laboratory of Solids Process Engineering, Emil-Figge-Str. 68, D-44227 Dortmund, Germany

A B S T R A C T

Supersaturation profiles of amorphous indomethacin in aqueous solution containing 0.4 wt% and 4 wt% of isopropanol were predicted by combining separately-determined kinetics for dissolution, solution crystallization, and solid-state transformation. The kinetics of solid-state transformation were measured and compared to various data from the literature. The proposed kinetic model accounts for dissolution, solution crystallization and amorphous-to-crystalline solid-state transformation. It was validated for different initial amounts of amorphous and crystalline material and systems with different isopropanol contents. Furthermore, the influence of poly-ethylene glycol on the supersaturation behavior was investigated. The results clearly show the robustness of the model and give insight into the interplay of dissolution, solution crystallization, and solid-state transformation of. In particular, the influence of solid-state transformation on the overall supersaturation profile was elucidated in a quantitative manner. An amorphicity function $\varphi(t)$ is proposed to account for the kinetics of the solid-state transformation. Its general form could be derived consistently from different sets of experimental data and seems to be independent of the particle size of the amorphous material and hydrodynamic conditions. This work is among the first of its kind to successfully integrate dissolution, crystallization from solution and solid-state transformation in a model that shows good predictability.

1. Introduction

Low bioavailability is a major challenge in the pharmaceutical development of new active pharmaceutical ingredients (APIs). In many cases, the limiting factor is the low aqueous solubility of the crystalline API. A promising workaround is the usage of amorphous formulations. When dissolving such amorphous formulations in water, often a characteristic supersaturation profile is observed. The concentration increases sharply and surpasses the crystalline solubility. This is known as the solubility advantage of the amorphous state (Hancock and Parks, 2000; Paus et al., 2015a; Murdande et al., 2010). However, the supersaturated solution is prone to nucleation and crystal growth. Consequently, the supersaturation is only short-lived and plummets back to the crystalline-solubility limit. This characteristic concentration profile is often denominated as *spring-and-parachute* (Guzmán et al., 2007).

Alonzo et al. (2010), postulated that this is a result of the interplay of four contributions: Dissolution from the amorphous state, nucleation from the supersaturated solution, crystal growth from the supersaturated solution, and solid-state transformation of the amorphous solid. Polymeric excipients, which are often used to improve the performance of APIs, may affect each of these contributions. A number of models have been developed to better understand and model dissolution kinetics of crystalline and amorphous APIs (Noyes and Whitney, 1897; De Almeida et al., 1997; Ji et al., 2015) as well as release kinetics (Higuchi, 1961; Higuchi, 1963; Korsmeyer et al., 1983). Polymers were shown to have kinetic and thermodynamic effects on dissolution.

Obtaining reliable nucleation kinetics remains a challenging task. Still, some work exists in the literature that uses classical nucleation theory to model nucleation. The role of polymers as nucleation inhibitors was investigated by different authors (Cheng et al., 2019; Abbou Oucherif et al., 2013). Langham et al. (2012) found out that during dissolution of amorphous tablets of felodipine (FEL) crystal seeds are generated due to erosion of the tablet. Therefore, they argued that the desupersaturation of the solution is essentially governed by growth of

those seeds, whereas nucleation kinetics can be neglected. A similar argumentation is proposed by a recent publication of Moseson et al. (2020).

Crystal-growth kinetics from solution were e.g. studied by the group of Taylor (Alonzo et al., 2010; Abbou Oucherif et al., 2013; Alonzo et al., 2012; Schram et al., 2016; Patel and Anderson (2014); Patel and Anderson (2015)) and Cheng et al. (2019), for a variety of APIs. Kinetic effects of hydroxypropylmethycellulose (HPMC) and poly-vinylpyrrolidone (PVP) were observed consistently. In a previous publication (Schneider et al., 2020), we investigated the crystal-growth kinetics of naproxen (NAP) and indomethacin (IND) in the presence of pre-dissolved polyethylene glycol (PEG) and were able to show a purely thermodynamic effect exerted by the polymer, meaning that PEG only influenced the aqueous NAP and IND solubility.

Amorphous substances in contact with water vapor usually undergo phase transformation. Andronis et al. (1997), showed that indomethacin when exposed to a humid environment transforms from the amorphous to the crystalline state. Depending on the relative humidity, different polymorphs are formed. At lower relative humidity the more stable γ-polymorph was observed while at high relative humiditiy the α-polymorph appeared. Similar observations have been made for many APIs. It is commonly assumed that the amorphous solid absorbs water and leads to a lowering of the glass-transition temperature and thereby to an increase of molecular mobility within the solid. This gives rise to crystallization. Such transformations are usually detected by PXRD, Raman spectroscopy, polarized light microscopy or DSC. Wu and Yu (2006), reported that the surface-crystallization rate of amorphous IND is by orders of magnitude greater than the bulk-crystallization rate.

Fewer data exists in the literature on the transformation of amorphous substances when in contact with liquid water. To assume that this behavior can be extrapolated from water-sorption data at high relative humidity seems questionable as different mechanisms may be at play when liquid water is present. For instance, in the latter case, dissolution is occurring at the same time and could affect sorption kinetics. Nova-kovic et al. (2020), qualitatively showed that amorphous forumulations of IND/PVP exhibited considerable surface crystallinity after exposure to water for 45 min during dissolution testing. Surwase et al. (2013), used IR spectroscopy to characterize amorphous IND after it was in contact with liquid water for specific durations. Crystalline and amorphous IND have different IR spectral bands, thus allowing a differentiation between them. In fact, in their work, they developed a principal component analysis, which allowed identification of the amorphous state, various crystalline polymorphs as well as intermediates. At 298.15 K and pH 4.5, amorphous IND underwent transformation to the α-polymorph. Interestingly, this transformation occurred within hours rather than days as expected from extrapolation of the sorption-induced crystallization at high relative humidities. This suggests that such transformation kinetics need to be accounted for when modelling the supersaturation behavior. Alonzo et al. (2010), arrived at the same conclusion by using Raman spectroscopy for similar investigations for FEL and IND. They also included pre-dissolved HPMC and PVP in their investigations and concluded that these polymers inhibit the solid-state transformation. Intrinsic dissolution experiments of IND were conducted by Greco and Bogner (2010), as well as Savolainen et al. (2009). They showed that dissolution rates of amorphous indomethacin are initially much higher than the ones of the crystalline solid. However, within less than an hour, the dissolution rate started to drop and ultimately reached almost the same rate as the crystalline material. This also suggests that transformation is happening at a much faster rate than expected from vapor-sorption data.

To model supersaturation profiles, an overall model has to be developed that integrates all of these processes simultaneously. Lindfors et al. (2007), reported a successful modelling of simultaneous dissolution and crystal growth of FEL. In this work, we set out to develop and parameterize an overall model to describe and predict the supersaturation profile of amorphous IND. Following the argumentation of Langham et al. (2012), we will neglect nucleation and only consider dissolution of amorphous solid, crystal growth from solution, and solid-state transformation. Accordingly, in this work, a four-stage concept was developed. First, dissolution and seeded desupersaturation experiments were conducted separately. Second, dissolution and crystal-growth models were parameterized by fitting to the experimental dissolution and desupersaturation profiles, respectively. Third, the so-obtained kinetic models were combined to predict supersaturation profiles for dissolution and crystal growth happening simultaneously. In a final, fourth step, an experiment was performed in which dissolution and crystal growth occur at the same time to validate the prediction made in the previous step.

Special focus will be placed on how the kinetics of solid-state transformation influences the obtained supersaturation profiles. We will show how such kinetics can be derived from different literature data as well as from measurements performed in this work and compare the results. Ultimately, we show how the influence of pre-dissolved PEG can be included in this setup, where we build on our understanding of PEG obtained in our previous publication (Schneider et al., 2020). This work proposes a time-resolved integration of dissolution, crystallization from solution, and solid-state transformation kinetics to describe supersaturation profiles of APIs and adds to a hitherto small body of comparable literature work (Guo et al., 2018; Hirai et al., 2017; Nogami et al., 1969).

2. Theory

We follow a simplified approach of the population-balance approach of Randolph and Larson (1971) for a system of non-interacting particles that either shrink (dissolution) or grow (crystal growth). It is assumed that other source or sink contributions, agglomeration and breakage can be neglected. For simplicity sake it is further assumed that particles are uniform. The equations for non-uniform particles can be found in the supporting information.

2.1. Dissolution in the absence of crystalline seeds

The mass balance between the bulk molality $\tilde{m}^B$ of dissolved particles and the dissolution of amorphous particles is given by:

$$\frac{d\tilde{m}^B(t)}{dt} = -\frac{4\,\pi\,\rho_A\,N_{T,A}}{3\,M\,m_{sol}}\frac{dr_A^3(t)}{dt} \tag{1}$$

Here, ρ_A represents the mass-volume density, $N_{T,\,A}$ represents the total particle number, M represents the molecular mass of IND, m_{sol} represents the mass of solvent (i.e. solution exept IND) and r_A represents the particle radius of amorphous API.

Dissolution causes a reduction in particle radius.

$$\frac{dr_A(t)}{dt} = -\frac{M}{\rho_A}\varphi(t)\,J_D(t) \tag{2}$$

The rate of change of particle size r_A relates the amorphicity function $\varphi(t)$ and the dissolution rate $J_D(t)$. The dissolution rate $J_D(t)$ is adapted from the *chemical-potential-gradient model* of Ji et al. (2015). This includes a kinetic rate constant $k_{t,\,D}$ and the fundamental thermodynamic driving force, which is given by the difference between the chemical potential of the API in solution in equilibrium with the amorphous solid (SL(A)) and the chemical potential of the API in the bulk phase (B). API molalities $\tilde{m}$ are used as a measure of API concentration and molality-based activity coefficients of the API $\gamma_{\tilde{m}}$ are introduced to account for non-ideal behavior in the mixture. Additionally, a dissolution order g_D is introduced.

$$
\begin{aligned}
J_D(t) &= k_{t,D}\left[\frac{\mu^{SL(A)} - \mu^B(t)}{R\,T}\right]^{g_D} = k_{t,D}\left[ln\left(\frac{a^{SL(A)}}{a^B(t)}\right)\right]^{g_D}\\
&= k_{t,D}\left[ln\left(\frac{\gamma_{\tilde{m}}^{SL(A)}\,\tilde{m}^{SL(A)}}{\gamma_{\tilde{m}}^{B}(\tilde{m}^B)\,\tilde{m}^B(t)}\right)\right]^{g_D}
\end{aligned}
\tag{3}
$$

Here, $\tilde{m}^{SL(A)}$ represents the so-called amorphous solubility. The amorphicity function $\varphi(t)$ is a strictly concave function with values between unity at $t=0$ and zero. It accounts for the solid-state phase transformation from amorphous to crystalline material.

A system of differential equations can be constructed from Eqs. (1)–(3).

$$\frac{d\tilde{m}^B(t)}{dt} = \frac{4\,\pi\,N_{T,A}}{m_{\text{sol}}} r_A(t)^2 \varphi(t)\, J_D(t)$$
$$\frac{dr_A(t)}{dt} = -\frac{M}{\rho_A} \varphi(t)\, J_D(t) \tag{4}$$

To solve the differential equation system (Eq. (4)) initial conditions are needed. The initial value of $\tilde{m}^B$ is zero. The initial value of $r_A(t)$ has to be determined experimentally or estimated.

$$\tilde{m}^B(t=0) = 0$$
$$r_A(t=0) = r_{A,0} \tag{5}$$

The value of $N_{T,A}$ is related to the initial mass of amorphous particles m_A and the initial value $r_{A,0}$.

$$N_{T,A} = \frac{3\,m_{A,0}}{4\,\pi\,\rho_A\,r_{A,0}^3} \tag{6}$$

2.2. Desupersaturation in the presence of crystalline seeds

For modelling desupersaturation in the presence of crystalline seeds, a model setup can be used that is similar to the one presented above for dissolution.

$$\frac{d\tilde{m}^B(t)}{dt} = -\frac{4\,\pi\,N_{T,C}}{m_{\text{sol}}} r_C(t)^2 J_C(t)$$
$$\frac{dr_C(t)}{dt} = \frac{M}{\rho_C} J_D(t) \tag{7}$$

Here, ρ_C represents the mass-volume density, $N_{T,C}$ represents the total particle number of crystalline API particles. The crystallization rate $J_C(t)$ is adapted from the *chemical-potential-gradient model* of Ji et al. (2015). It includes a kinetic rate constant $k_{t,C}$ and the fundamental thermodynamic driving force, which is given by the difference between the chemical potential of the API in the bulk phase (B) and the chemical potential of the API which is in equilibrium with the crystalline solid (SL (C)). API molalities $\tilde{m}$ are used as a measure of API concentration and molality-based activity coefficients of the API $\gamma_{\tilde{m}}$ are introduced to account for non-ideal behavior in the mixture. Additionally, a growth order g_C is introduced.

$$J_c(t) = k_{t,C} \left[\frac{\mu^B(t) - \mu^{SL(C)}}{RT} \right]^{g_C} = k_{t,C} \left[ln\left(\frac{a^B(t)}{a^{SL(C)}} \right) \right]^{g_C}$$
$$= k_{t,C} \left[ln\left(\gamma_{\tilde{m}}^B(\tilde{m}^B) \frac{\tilde{m}^B(t)}{\gamma_{\tilde{m}}^{SL(C)}\,\tilde{m}^{SL(C)}} \right) \right]^{g_C} \tag{8}$$

To solve the differential equation system (Eq. (7)), initial conditions are needed. The initial value of $\tilde{m}^B$ is directly accessible from concentration measurements. The initial value of $r_C(t)$ has to be determined experimentally or estimated.

$$\tilde{m}^B(t=0) = \tilde{m}_0^B$$
$$r_C(t=0) = r_{C,0} \tag{9}$$

The value of $N_{T,C}$ is related to the initial mass of crystalline seeds m_C and the initial value $r_{C,0}$.

$$N_{T,C} = \frac{3\,m_{C,0}}{4\,\pi\,\rho_A\,r_{C,0}^3} \tag{10}$$

2.3. Dissolution in the presence of crystalline seeds

The supersaturation behavior can be modelled as a superposition of dissolution of amorphous particles and growth of crystalline seeds. It is assumed that amorphous and crystalline particles do not interact. A differential equation system can be constructed from the individual differential equations describing dissolution and crystal growth (Eqs. (4) and (7)).

$$\frac{d\tilde{m}^B(t)}{dt} = \frac{4\,\pi\,N_{T,A}}{m_{\text{sol}}} r_A(t)^2 \varphi(t)\, J_D(t) - \frac{4\,\pi\,N_{T,C}}{m_{\text{sol}}} r_C(t)^2 J_C(t)$$
$$\frac{dr_A(t)}{dt} = -\frac{M}{\rho_A} \varphi(t)\, J_D(t)$$
$$\frac{dr_C(t)}{dt} = \frac{M}{\rho_C} J_D(t) \tag{11}$$

It should be noted that this superposition is not a simple addition of dissolution and crystallization as the respective differential equations are coupled with one another by the bulk molality $\tilde{m}^B$. The initial conditions follow from Eqs. (5) and (9).

$$\tilde{m}^B(t=0) = \tilde{m}_0^B$$
$$r_A(t=0) = r_{A,0}$$
$$r_C(t=0) = r_{C,0} \tag{12}$$

It should be noted that the initial bulk molality $\tilde{m}_0^B$ is not zero but slightly higher due to dissolution from crystalline seeds before amorphous particles are added. The total numbers of amorphous particles $N_{T,A}$ and crystalline seeds $N_{T,C}$ are calculated according to Eqs. (6) and (10), respectively.

3. Materials and methods

3.1. Materials

Crystalline IND (γ-polymorph, purity $\geq$99%) was purchased from TCI Deutschland *Co.*, LLC (Eschborn, Germany). PEG 400 was purchased from Applichem (Darmstadt, Germany). Isopropanol (LC grade) was purchased from Merck KGaA (Darmstadt, Germany). All substances were used as obtained without further purification. Water was filtered, deionized, and distilled using a Millipore purification system and used for all experiments.

3.2. Preparation of amorphous IND

Amorphous IND was prepared by melt cooling. For that purpose, crystalline IND was melted at 453.15 K in a steel vessel before being rapidly transferred to another steel vessel pre-cooled to 278.15 K. The solid was crushed with a pre-cooled steel rod and later sieved through sieves with a 400 µm and 250 µm aperture mesh size. The amorphous particles were stored under vacuum at 298.15 K and used within 24 h.

3.3. Experimental setup for dissolution, desupersaturation, and supersaturation experiments

All experiments were conducted in a jacketed 75 mL glass reactor. Temperature was kept constant at 298.15 K with a water-cooled thermostat (Lauda 300E, Lauda, Königshofen, accuracy 0.2 K). Mixing was ensured by a magnetic stirrer (width of 2 cm) at a stirring speed of 460 rpm. Total solvent mass was 72 g. Samples were withdrawn, filtered through syringe filters (PTFE, 0.45 µm) and immediately diluted in isopropanol (ISO). Concentration of IND was determined by UV–vis spectroscopy at a wavelength of 319 nm.

3.4. Dissolution experiments in the absence of crystalline seeds

Appropriate amounts of amorphous particles was added rapidly into the equilibrated reactor, which was prepared as described in Section 3.3. Samples were withdrawn at regular intervals and analyzed as described in Section 3.3. Dissolution of amorphous particles was reproducible by 2% average relative standard deviation between biological duplicates, if the same batch of particles was used within 2 h (see Fig. S10). Due to longer storage and differences between batches (different kinetic history incurred during quench-cooling, different particle size distribution incurred during manual diminution), the overall reproducibility of dissolution profiles of amorphous particles decreases to approximately 12% average relative standard deviation between biological duplicates from different batches for these cases. Therefore, dissolution experiments in the absence and presence of crystalline seeds (see Section 3.6) were always performed with particles from the same batch.

3.5. Desupersaturation experiments in the presence of crystalline seeds

Appropriate amounts of crystalline seeds (6 or 9 mg) were added to the equilibrated reactor, which was prepared as described in Section 3.3. Ultrasound was applied by immersing the reactor in a sonicator (RK 100 SH, 35 kHz, 350 W, Bandelin, Berlin, Germany) set to 298.15 K for 120 s. After being replaced on the magnetic stirrer plate, supersaturation was generated by rapidly adding a small amount of solution (300 mg) of highly concentrated IND dissolved in ISO. Samples were withdrawn at regular intervals and analyzed as described in Section 3.3. Desupersaturation profiles were reproducible with an approximate average relative standard deviation of 2% between biological duplicates (see Fig. S10).

3.6. Dissolution experiments in the presence of crystalline seeds

Appropriate amounts of crystalline seeds were added to the equilibrated reactor. Ultrasound was applied by immersing the reactor in a sonicator (RK 100 SH, 35 kHz, 350 W, Bandelin, Berlin, Germany) set to 298.15 K for 120 s. After being replaced on the magnetic stirrer plate, appropriate amount of amorphous particles from the same batch as the corresponding seed-free dissolution experiment (see Section 3.4) was added rapidly. Samples were withdrawn at regular intervals and analyzed as described in Section 3.3.

3.7. Intrinsic-dissolution experiments

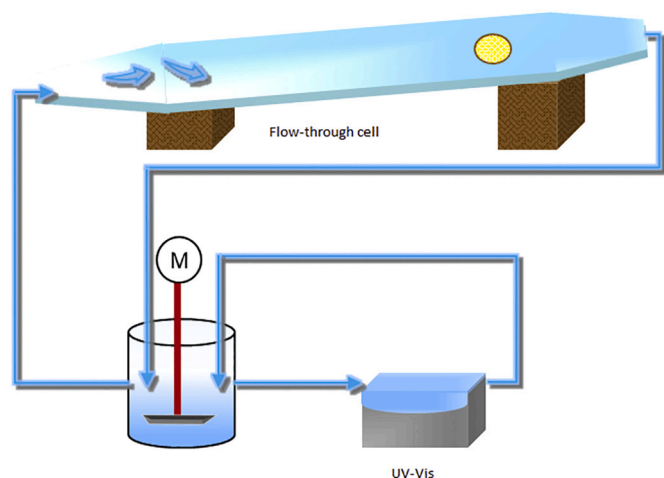Intrinsic-dissolution experiments were performed using a flow-

Fig. 1. Experimental setup for measurement of intrinsic dissolution rates used within this work.

through dissolution cell. The schematic setup is visualized in Fig. 1. The dissolution medium was water. IND was pressed into a cylindrical matrix with a diameter of 13 mm with a force of 10 kN. The matrix was than inserted into the bottom of the flow cell so that a flat, circular sample surface was exposed to the dissolution medium. The volumetric-flow rate was adjusted to 902 mL/min, which corresponds to a Reynolds number of 500 (viscosity of pure water at 298.15 K and a characteristic length of 167 mm). UV–vis absorption was measured at 319 nm. IND solid material in the cylinder matrix was recovered after the experiment for visual inspection.

3.8. Solubility experiments

Excess crystalline IND was added to the solvent system in a 50 mL jacketed glass vessel. Temperature was kept constant at 298.15 K with a water-cooled thermostat (Lauda 300E, Lauda, Königshofen, accuracy 0.2 K). Mixing was ensured by a magnetic stirrer. Samples were withdrawn, solid particles separated with syringe filters (PTFE, 0.45 μm), and analyzed with UV–vis spectroscopy at a wavelength of 319 nm. Equilibration time was at least 72 h. It was ensured that API concentrations has reached a stationary value.

3.9. Modelling

3.9.1. Concept

(1) The dissolving, amorphous particles were assumed as spherical and uniform, not to interact with other solid particles, and having a constant mass-volume density. The initial particle size is taken from the arithmetic mean of the aperture of lower and upper mesh used for sieving amorphous particles. The amorphous solubility was calculated from the crystalline solubility measured in the respective water/isopropanol system and multiplied with a solubility advantage factor of 4.4. This value is in general agreement with the solubility-advantage factor reported for IND at 298.15 K in pure water by various sources (Murdande et al., 2010; Murdande et al., 2011). We opted to use this experimental value, as theoretical calculation were shown to yield considerable overestimations (Murdande et al., 2010; Paus et al., 2015b). It was assumed that the presence of ISO does not affect this value. This assumption often holds for additives at low concentrations.

For all sets (dissolution experiment in the absence and presence of crystalline seeds), amorphous material from the same batch was used. This way, each set is consistent in itself and represented in the modelling by unique kinetic parameters for dissolution. Due to the limited reproducibility of dissolution profiles between different batches of amorphous IND (melting/cooling history, particle diminution), separate kinetic parameters were determined for different batches. This was done, so that errors from insufficient parameter fitting are minimized, as we were mainly interested in investigating whether the integration of dissolution, crystal growth and solid-state transformation is correctly predicted and not in the absolute values of the kinetic parameters themselves (nonetheless, we believe that the order of magnitude of the so-determined kinetics parameters should be reliable). The overall deviation of the kinetic parameters for dissolution across all batches is 15% and reflects the reproducibility of dissolution profiles from different batches (12%, see Section 3.7).

(2) It was assumed that liquid-bulk desupersaturation can only occur by growth of crystalline seed particles. In contrast, transformed crystalline regions of the formerly amorphous surface were assumed as being inaccessible to growth by liquid-bulk desupersaturation. This is legitimized by the fact that the total surface of crystalline seed particles was at least 5–10 times larger than the total surface area of amorphous particles.

The growing crystalline seed particles were assumed to be spherical and uniform, do not interact with other solid particles, and have a constant mass-volume density. The diameter of seed particles is estimated as 12.6 μm. This is in accordance with the sauter-mean diameter obtained from size-distribution measurements performed for similarly-prepared crystal-seed suspensions reported in our earlier publication (Schneider et al., 2020). The crystalline solubility (of the γ-polymorph) in the respective water/isopropanol systems was measured in separate solubility experiments. Particle growth was coupled with the total mass balance. The particle number and initial particle size were estimated from size-distribution measurements by laser diffraction.

(3) When predicting dissolution profiles of amorphous IND in the presence of crystalline seeds, it was assumed that crystal growth commences once the liquid-bulk concentration surpasses the crystalline solubility. During the short period before crystalline solubility was attained (less than 2 min), the crystalline seed particles were considered as being inert. The concentration of IND already dissolved immediately before adding of amorphous particles was determined in separate experiments and was 0.44×10^{-8} mol/g_{solv} in the 0.4 wt% ISO system and 0.67×10^{-8} mol/g_{solv} in the 4 wt% ISO system on average. However, in some cases (Fig. S5 and S8) starting concentrations seemed higher judging from the initial part of the measured dissolution profile in the presence of seeds (probably due to aberrations in the ultrasound performance). In these cases, the starting concentration was estimated by linear back extrapolation from the first and second data points of the measured dissolution profile. The correct starting concentration seems to be only relevant for the initial part of the predicted dissolution profile in the presence of crystalline seeds. Over time, the effect fades out and the predicted concentration profiles approach one another independent of the chosen starting concentration (see Fig. S11).

(4) The transformation of the amorphous surface to the crystalline state is represented in this work by a gradually-decreasing function called amorphicity $\varphi(t)$. It can be interpreted as the portion of the amorphous particle surface effectively accessible for dissolution. It has a value of one at the beginning of the experiment and decreases gradually. Once a value of zero is attained, dissolution ceases altogether.

(5) The ratio of activity coefficients (Eqs. (5) and (10)) was calculated using PC-SAFT. Parameters used for the modelling can be found in Tables S14 and S15. Theoretical details can be found in the supporting information of our previous publication (Schneider et al., 2020). It was observed that this ratio is very close to unity over the entire relevant concentration range (Fig. S13). This is in agreement with findings made for similar systems in our earlier publication (Schneider et al., 2020) as well as that by Paus et al. (2015b). It is reasonable, because the concentrations are very small, so that the activity coefficients are very close to the infinite dilution activity coefficient of IND in the water/ISO solvent at 298.15 K.

3.9.2. Sensitivity analysis

The modelling (Eqs. (3)–(6) and (7)–(10)) and predictions (Eqs. (11) and (12)) depend on a plethora of input quantities (see Table 1), namely density, volume shape factor, initial particle size, total particle number, and solubility for the amorphous and the crystalline particles. Due to the strategy of optimizing kinetic parameters from separate dissolution and desupersaturation profiles, where the same input quantities were used as in the subsequent predictions of supersaturation profiles, internal error compensation was likely to occur. This was exploited to ascertain by which error margin the above-named input quantities had to be

Table 1

Input quantities for modelling with Eqs. (3)–(6), (7)–(10), and (11)–(12).

Quantity	Value	Notes
M [g/mol]	357.79	
ρ_A [g/m^3]	1,320,000	
ρ_C [g/m^3]	1,400,000	
$\tilde{m}^{SL(A)}$ (w_{ISO} = 0.4%) [10^{-8} mol/g_{solv}]	7	a
$\tilde{m}^{SL(A)}$ (w_{ISO} = 4%) [10^{-8} mol/g_{solv}]	9.6	a
$\tilde{m}^{SL(A)}$ (w_{ISO} = 4%, $w_{PEG\ 400}$ = 0.5%) [10^{-8} mol/g_{solv}]	12.2	a
$\tilde{m}^{SL(C)}$ (w_{ISO} = 0.4%) [10^{-8} mol/g_{solv}]	1.6	Measured in this work
$\tilde{m}^{SL(C)}$ (w_{ISO} = 4%) [10^{-8} mol/g_{solv}]	2.2	Measured in this work
$\tilde{m}^{SL(C)}$ (w_{ISO} = 4%, $w_{PEG\ 400}$ = 0.5%) [10^{-8} mol/g_{solv}]	2.8	Measured in this work
$r_{A,\ 0}$ [m]	162.5×10^{-6}	b
$r_{C,\ 0}$ [m]	6.3×10^{-6}	c

[a] Calculated from crystalline solubility and a solubility advantage factor of 4.4.
[b] Delta-shaped distribution around average between upper and lower sieve mesh aperture.
[c] Delta-shaped distribution around sauter-mean diameter obtained from laser-diffraction measurement.

predetermined. To that end, a sensitivity analysis was performed with respect to the various input quantities. It was found that all above-named input quantities can be varied by at least 10% without affecting the prediction of the supersaturation profiles. This affirmed the assumption of internal error compensation and gave certain leeway within physically-realistic thresholds for the values of the input quantities. Care must of course be taken, when amorphous or crystalline solubility is approached. This is particularly important for the value of the amorphous solubility, which is discussed heatedly in the literature. The herein used value of 7×10^{-8} mol/g_{solv} corresponds to the often cited range of 20–25 mg/L at 298.15 K in water (Alonzo et al., 2010). This agrees with the solubility advantage factor of 4.4 used in this work and reported from experimental work of other authors (Murdande et al., 2010; Murdande et al., 2011). In a recent work Štukelj et al. (2019) reported a considerably higher solubility advantage factor of 20.8. This value is close to the value obrained from theoretical free energy difference calculations. In any case, the herein observed internal error compensation and the fact that the herein measured concentrations were always below this threshold value should minimise the effect of potential error in the assumed amorphous solubility.

4. Results

4.1. Dissolution profiles of amorphous IND in water/ISO at 0.4 wt% ISO

Fig. 2 shows the dissolution, desupersaturation, and supersaturation profiles of 30 mg amorphous IND in the presence of 9.9 mg crystalline seeds in a water/isopropanol (w_{ISO} = 0.4%) system at 298.15 K and 460 rpm. The experimental dissolution profile shows a typical increase in concentration. At the outset, it is almost linear, while later on, the slope decreases as the concentration approaches the amorphous solubility limit $\tilde{m}^{SL(A)}$. At 2400 s, a peak concentration of approximately 6×10^{-8} mol/g_{solv} is reached after which the concentration decreases rapidly. This observed profile can be explained as follows: First, the increase in concentration reduces the thermodynamic driving force for dissolution. Second, as the particles dissolve, they experience shrinkage and thus their surface is decreasing. Third, after some time (presumably at around 2000 s judging from visual inspection), when a certain supersaturation is achieved, nucleation and crystal growth from the liquid bulk may commence. The combined effect of these three factors causes the
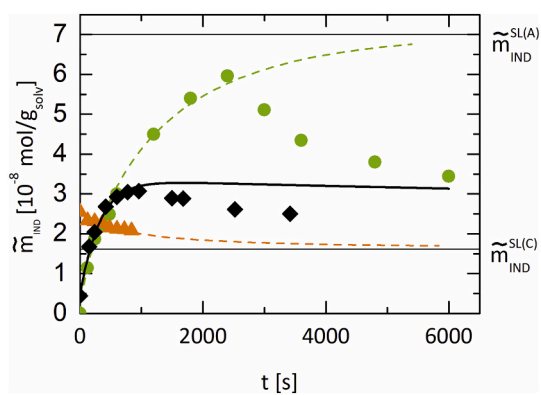
Fig. 2. Dissolution profile of 30 mg amorphous IND (circles), desupersaturation profile by growth of 9 mg crystalline IND seeds (triangles), and dissolution profile of 30 mg amorphous IND in the presence of 9 mg crystalline IND seeds (diamonds). All experiments were performed in water/ISO (w_{ISO} = 0.4%) at 298.15 K and 460 rpm. ISO was used to generate the initial supersaturation in the crystal-growth experiment. For consistency, it was used in the same concentration in the dissolution experiments as well. Dashed lines represent fits obtained with model Eqs. (3)–(6) (dissolution) and Eqs. (7)–(10) (desupersaturation). The solid line represent a predictions of the simultaneous dissolution of amorphous IND and growth of crystalline seeds according to Eqs. (11) and (12) without considering amorphous surface transformation.

dissolution profile to deviate from the initial linear trajectory. When dissolution and nucleation/crystal growth occur at equal rates the maximum concentration is observed. After that, desupersaturation overpowers dissolution and the liquid-bulk concentration drops. Extrapolating the initial profile gives the impression that the concentration is headed towards the amorphous solubility limit $\tilde{m}^{SL(A)}$, if nucleation/crystal growth were not to interfere. This further validates the assumed value of the amorphous solubility limit of 7×10^{-8} mol/g_{solv}.

The desupersaturation profile shows the expected decrease towards equilibrium crystalline solubility starting from an initial supersaturation. Although the experiment was not performed until equilibrium was reached, the course still suggests that equilibrium would be attained eventually. The supersaturation experiment shows almost the same initial increase as the dissolution experiment. Note that unlike the latter, it starts from a higher concentration (0.44×10^{-8} mol/g_{solv}) which is due to the seed crystals dissolving partly during pre-experimental sonication. The initial slope, however, is almost the same in both experiments. This meets the expectations, as crystal growth is negligible at the outset of the experiment when concentration is low.

The supersaturation experiment exhibits a peak concentration of approximately 3×10^{-8} mol/g_{solv} at 1000 s. It is lower in value than the peak of the dissolution experiment ($5.5 \times$ mol/g_{solv}) and occurs earlier. This is reasonable, as the crystal growth of the crystalline seeds in the supersaturation experiments represents an additional sink term for the liquid-bulk concentration and therefore acts as an antagonist to the dissolution of amorphous particles. After reaching the peak, the concentration drops. Although the supersaturation experiment was not conducted long enough to observe the concentration reaching the assumed crystalline solubility of 1.6×10^{-8} mol/g_{solv}, the course suggests that this would eventually be the case. It should be noted that the supersaturation profile is asymmetric with respect to the peak in the sense that the initial concentration increase is faster than the subsequent decrease.

The dissolution kinetic parameters $k_{t,\,D}$ and g_D were obtained by fitting the dissolution model (Eqs. (3)–(6)) to the experimental dissolution profile of amorphous IND until 1200 s (Fig. 2). The parameters are listed in Table 4. Visual inspection revealed that at 2000 s newly formed crystalline particles appeared. Before that, the concentration evolution

can be assumed as being dominated by dissolution. The crystal-growth kinetic parameters $k_{t,\,C}$ and g_C were determined by fitting the crystal-growth model (Eqs. (7)–(10)) to the experimental desupersaturation curve.

These kinetic parameters were used to generate a prediction of the supersaturation profile (Fig. 2), where dissolution of amorphous particles and crystal growth of seed particles coincide. Interestingly, the peak concentration (3.2×10^{-8} mol/g_{solv} instead of 3.0×10^{-8} mol/g_{solv}), and time (1200 s instead of 1000 s) is only slightly overestimated. More drastically, the subsequent decline in concentration is not at all captured. While the experimental supersaturation profile decreases considerably after reaching the peak, the prediction shows only a very slow decrease.

This behavior of the model can be reasoned from inspecting the rates of dissolution and crystal growth in the context of changing thermodynamic driving force and surface areas. In the initial part of the supersaturation experiment, the concentration increases fast towards the amorphous solubility. Thus, the driving force for dissolution is decreasing. Additionally, the surface area of the amorphous particles decreases due to shrinkage in the course of dissolution. In combination, the dissolution rate decreases. In contrast, the crystal-growth rate increases, as the concentration increases away from the crystalline solubility and particles experience growth. Consequently, the crystal-growth rate soon equals the dissolution rate and the peak of the supersaturation profile is reached. As the concentration drops after the peak, amorphous particles continue to dissolve (surface area decreases). However, the thermodynamic driving force increases again. Conversely, crystalline particles continue to grow (surface area increases) but the thermodynamic driving force decreases. Thus, the rates do not change as fast as in the initial part prior to the peak. Consequently, the predicted liquid-bulk concentration only decreases slowly.

The fact that the initial part – especially the peak – is surprisingly well predicted by combining the individual kinetics of dissolution and crystal growth from solution, corroborates that the kinetics are in general correctly integrated with one another. Apparently, as time progresses, the situation changes and something is obviously unaccounted for by the modelling. Either, dissolution is overestimated in the later part of the experiment or crystal-growth is underestimated. It could be speculated that the presence of the amorphous particles could serve as secondary nucleary sites. However, the crystal-seed loading was consciously chosen to be very high (approximately 1.3), thereby exhibiting a comparably large surface area of seeds. In combination with the moderate supersaturation factor observed during the experiment (less than factor of 2), the effect of secondary nucleation should be very small and desupersaturation should be essentially dominated by crystal growth. It thus seems rather likely that dissolution is overestimated by the model. Amorphous-to-crystalline solid-state transformation, which gradually reduces the dissolution performance, could explain this finding. A way to improve the prediction is therefore offered by including transformation kinetics of the amorphous solid, which is discussed further in the following section.

4.2. Quantification of amorphous-to-crystalline solid-state-transformation kinetics of IND by means of phi functions

Amorphous-to-crystalline solid-state-transformation kinetics of IND represented by amorphicity functions $\varphi(t)$ were derived in this work from different experiments reported in literature, as well as from own measurements. Greco and Bogner (2010) published intrinsic dissolution rates of melt-quenched IND in water at approximately 295.15 K. The surface area was kept constant by exposing only a flat circular area to the solvent. Thermodynamic driving force was also constant, as ensured by a flow-through setup. They evaluated the dissolution rates of the amorphous solid over time, as well as that of the crystalline solid. They observed that the dissolution rate of the amorphous solid decreases from a high value towards a low value close to the dissolution rate of the

crystalline solid, which then remained constant. By relating the dissolution rates of amorphous $R_D^{(A)}(t)$ and crystalline $R_D^{(C)}$ IND reported by Greco and Bogner, an amorphicity function $\varphi(t)$ was derived in this work using the following expression:

$$\varphi_{\text{Greco}}(t) = \frac{R_D^{(A)}(t) - R_D^{(C)}}{R_D^{(A)}(0) - R_D^{(C)}} \qquad (13)$$

A similar measurement at 298.15 K was performed in this work. The results are shown in Fig. 3. It can be seen that the dissolution rate (i.e. slope) of the amorphous solid decreases over time until it reaches the same slope as the crystalline counterpart after approximately 10,000 s. Note, that the dissolution rate of the amorphous solid starts decreasing considerably already after 1500 s. This time point matches the time when the supersaturation prediction in Fig. 2 starts to fail. The amorphicity function $\varphi_{\text{Schneider}}(t)$ was derived from these experimental data as described for the data of Greco and Bogner in Eq. (13). Table 4 lists the exact equations used for the various phi functions.

Further data of amorphous-to-crystalline solid-state transformation are accessible from the publication of Surwase et al. (2013). The IR data reported therein suggests that the transformation of melt-quenched indomethacin in water at a pH value of 4.5 and 298.15 K can be projected as a movement along a principal component (PC) axis. By applying a simple lever law between the endpoints represented by the initial amorphous material $PC^{(A)}(0)$ and the final α-polymorph $PC^{(C)}$, an amorphicity function $\varphi_{\text{Surwase}}(t)$ was derived.

Fig. 4 shows the amorphicity functions $\varphi(t)$ derived from the data of Greco and Bogner for two different flow rates (0.5 and 7 ml/min) and the one of Surwase compared to the measurements performed in this work. It can be noted that they all are in general agreement. They show a drastic decrease to a value of 0.5 within the first 300 s. This means that the active amorphous surface underwent phase transformation to the crystalline state much faster than expected from the extrapolation of water-sorption data at high relative humidities as reported by Andronis et al. (1997). Interestingly, this agrees with the work of Langham et al. (2012), who postulated that for 5 wt% FEL/PVP formulation, only 50% of FEL mass is released as amorphous particles, while the rest erodes as transformed crystalline particles. Similarly, for a 15 wt% FEL/PVP formulation, only 11% of FEL mass is released as untransformed amorphous material. From the PXRDs of the formulations at the outset of their experiments, there was no indication of initial crystallinity. The postulated transformation, incidentally also on the same time scale as the experiments performed in this work, seems to be caused by direct exposure to liquid water. In this work, for the first time, we quantify the time evolution of amorphicity. The fact that $\varphi(t)$ represents a fractional active surface allows that they are independent of particle size and can be directly compared between different works as long as the conditions are similar with respect to temperature and pH. Hydrodynamic conditions seem to have little effect, as they were considerably different in the
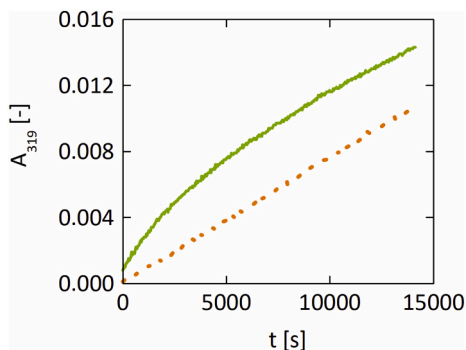

Fig. 3. UV–vis absorbance at 319 nm of intrinsic dissolution measurements of amorphous (solid line) and crystalline (dotted line) IND in water at 298.15 K and a flow rate of 902 mL/min.
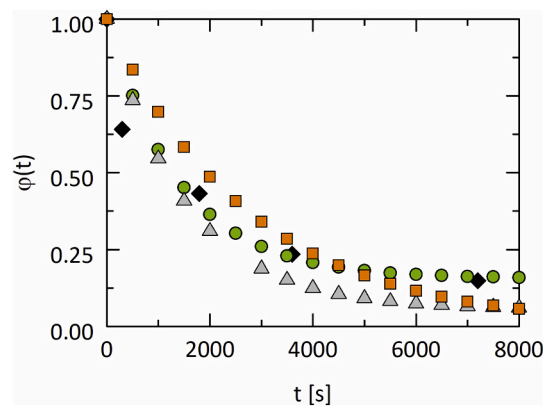

Fig. 4. Amorphicity functions $\varphi(t)$ derived from intrinsic dissolution rate data of Greco and Bogner at 295.15 K and flow rates of 7 ml/min (circles, hereinafter denominated as $\varphi_{\text{Greco, 7}}$) and 0.5 ml/min (triangles, hereinafter denominated as $\varphi_{\text{Greco, 0.5}}$), measurements performed in this work at 298.15 K and a flowrate of 902 ml/min (squares, hereinafter denominated as $\varphi_{\text{Schneider}}$) and IR data of Surwase (diamonds, hereinafter denominated as φ_{Surwase}) at 298.15 K and pH of 4.5.

various measurements.

It should be noted that the evaluation of amorphicity functions from dissolution rate data bears intricacies, as they heavily depend on the initial dissolution rate. It is reported in literature that during intrinsic-dissolution-rate measurements, surface smoothing occurs, which affects measured dissolution rates, particularly at the outset of the experiment. The derived amorphicity functions are therefore to be regarded as estimates. Likewise, the amorphicity function derived from the IR data of Surwase et al. has to be put into perspective of the errors reported for the principal component analysis, which are in some cases quite large. This is due to the thickness of the transformed crystalline surface, which is presumably very small compared to the total particle size. Thus, only a fraction of the convoluted IR signal corresponds to the amorphous surface regions.

4.3. Including amorphous-to-crystalline solid-state-transformation kinetics in the modelling of dissolution profiles of amorphous IND in water/ISO at 0.4 wt% ISO

Kinetic dissolution parameters under the premise that surface transformation is occurring were determined by fitting Eqs. (3)–(6) to the initial part of the dissolution profile of amorphous IND (Fig. 2). The amorphicity function derived from the data of Greco and Bogner at 7 mL/min $\varphi_{\text{Greco, 7}}(t)$ was chosen, because it represents a good compromise of the different phi functions. However, the different amorphicit functions yield similar results when used for predicting dissolution profiles of amorphous IND in the presence of crystalline seeds (see Fig. S12). Note that g_D is reduced, while $k_{t, D}$ is increased when surface transformation is accounted for by the phi function $\varphi(t)$ derived from the literature (cf Tables 2 and 3). This is expressed in Eq. (16) where the dissolution rates with and without consideration of surface transformation have to be the same.

$$\frac{D^*}{D} = 1 = \varphi(t) \frac{r^*(t)^2}{r(t)^2} \frac{k_{t,D}^*}{k_{t,D}} \Gamma(t)^{g_D^* - g_D} \qquad (14)$$

The asterisk symbol (*) marks the quantities obtained when accounting for surface transformation. The time dependency of the amorphicity function $\varphi(t)$ has to be mainly compensated by a change of the growth factor from g_D to g_D^* as the radius time evolution should be very similar for both cases due to the large particle size and comparably small size changes. As the thermodynamic driving force $\Gamma(t)$ is generally smaller than unity, g_D^* has to be smaller than g_D.

Table 2

Kinetic parameters and average relative deviations (ARDs) between experimental data and predictions using the amorphicity function $\varphi_{\text{Greco, 7}}(t)$ to account for amorphous-to-crystalline solid-state transformation.

Experiment[a]	Figure/ Symbol[b]	$k_{t,\,D}$ [10−6 mol/m²s]	g_D [−]	$k_{t,\,C}$ [10−6 mol/m²s]	g_C [−]	ARD [%]
30/9/4/0	8/Circles 9/Squares	8.0	0.6	2.0	1.6	7.4
30/9/4/0.5	9/Circles	4.0	0.4	2.0	1.6	5.1
20/9/0.4/0	7/ Diamonds 6/ Diamonds	6.3	0.4	1.8	2.0	4.9
20/6/0.4/0	7/Circles	8.0	0.4	1.8	2.0	5.7
30/9/0.4/0	2/ Diamonds 5/ Diamonds 6/Circles 8/ Diamonds	9.0	0.5	1.8	2.0	4.5

[a] Nomenclature: Amorphous mass [mg]/crystalline mass [mg]/wt% of ISO/ wt% of PEG 400.

[b] Indicates the Figure number as well as the experimental data set to which the prediction belongs.

Table 3

Kinetic parameters and average relative deviations (ARDs) between experimental data and predictions without accounting for amorphous-to-crystalline solid-state transformation (i.e. $\varphi(t) = 1$).

Experiment[a]	Figure/ symbol[b]	$k_{t,\,D}$ [10−6 mol/m²s]	g_D [−]	$k_{t,\,C}$ [10−6 mol/m²s]	g_C [−]	ARD [%]
30/9/4/0	8/Circles 9/Squares	6.0	0.9	2.0	1.6	17.8
30/9/4/0.5	9/Circles	3.0	0.8	2.0	1.6	11.2
20/9/0.4/0	7/ Diamonds 6/ Diamonds	3.5	1.0	1.8	2.0	5.8
20/6/0.4/0	7/Circles	5.0	0.8	1.8	2.0	5.5
30/9/0.4/0	2/ Diamonds 5/ Diamonds 6/Circles 8/ Diamonds	6.5	0.8	1.8	2.0	11.5

[a] Nomenclature: Amorphous mass [mg]/crystalline mass [mg]/wt% of ISO/ wt% of PEG 400.

[b] Indicates the Figure number as well as the experimental data set to which the prediction belongs.

Fig. 5 shows the improved prediction of the dissolution profile of amorphous IND in the presence of crystalline IND seeds obtained when accounting for the amorphous-to-crystalline solid-state-transformation kinetics by using the $\varphi_{\text{Greco, 7}}(t)$ amorphicity function. It can be seen that in comparision to Fig. 2, where to solid-state transformation was neglected (i.e. $\varphi(t)=1$), the prediction now is in excellent agreement

with the experimental dissolution profile over the entire course.

It should be noted that the predictions of dissolution profiles in the presence of crystalline seeds with and without surface transformation start to deviate at around 900 s (compare Figs. 2 and 5). At the first glance, this might be surprising because the dissolution parameters were fitted so that they describe the dissolution profile of IND in the absence of crystalline seeds equally good until 2000 s, irrespective of the amorphicity function used. However, this information is critical in assessing the influence of the amorphicity function. As both dissolution fits are equally-good descriptions of the experimental dissolution profile in this time range, the fact that only when using the correct amorphicity function one obtains a good prediction of the supersaturation profile underscores that the dynamics of dissolution, solution crystallization, and surface transformation are correctly integrated with one another. The reason, why the predictions of dissolution profiles in the presence of crystalline seeds differ already considerably depending on whether or not solid-state transformation is accounted for, while the dissolution profiles in the absence of crystalline seeds are equally well described, lies in the fact that the time evolution of the amorphicity function becomes detached from time evolution of the thermodynamic driving force when combining dissolution and solution crystallization. The kinetic parameters of dissolution (Tables 2 and 3) were optimized individually with and without surface transformation so that they yield the same slope for the given concentration-time profile. Thus, the amorphicity function is coupled to the specific time evolution of the thermodynamic driving force from the dissolution profile, which is imparted on the
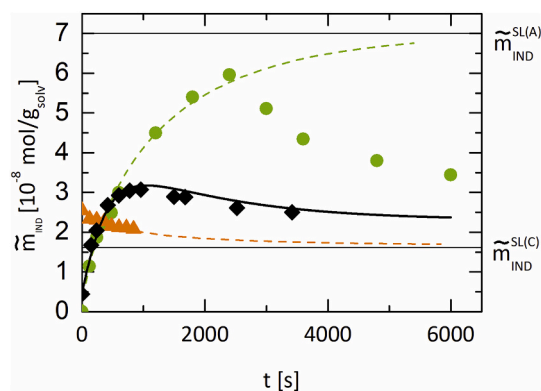

Fig. 5. Dissolution profile of 30 mg amorphous IND (circles), desupersaturation profile by growth of 9 mg crystalline IND seeds (triangles), and dissolution profile of 30 mg amorphous IND in the presence of 9 mg crystalline IND seeds (diamonds). All experiments were performed in water/ISO ($w_{\text{ISO}} = 0.4\%$) at 298.15 K and 460 rpm. ISO was used to generate initial supersaturation in the crystal growth experiment. For consistency, it was used in the same concentration in the dissolution experiments as well. Dashed lines represent fits obtained with model Eqs. (3)–(6) (dissolution) and (7)–(10) (desupersaturation). The solid line represent a predictions of the simultaneous dissolution of amorphous IND and growth of crystalline IND seeds according to Eqs. (11) and (12) with considering amorphous surface transformation by the amorphicity function $\varphi_{\text{Greco, 7}}(t)$ derived from the intrinsic-dissolution-rate data of Greco and Bogner at a flow rate of 7 mL/min.

Table 4

Amorphicity function $\varphi(t)$ of quench-cooled amorphous IND in water at 298.15 K.

Name	Mathematical expression	Flow rate	Experimental data
$\varphi_{\text{Greco, 7}}$	$\left(3.3 \cdot exp\left(-\dfrac{t}{23.8 \cdot 60}\right) + 1.39 - 0.78\right)\big/(4.69 - 0.78)$	7 mL/min	Greco and Bogner (2010)
$\varphi_{\text{Greco, 0.5}}$	$\left(2.7 \cdot exp\left(-\dfrac{t}{25.4 \cdot 60}\right) + 0.42 - 0.26\right)\big/(3.12 - 0.26)$	0.5 mL/min	Greco and Bogner (2010)
$\varphi_{\text{Schneider}}$	$\left(exp\left(-\dfrac{t}{8900}\right)\right)^{3.2}$	902 mL/min	This work
φ_{Surwase}	$-0.00119601 \cdot t + 1$ for $t < 300$ s $-0.15839123 \cdot \ln(t) + 1.56255692$ for $t \geq 300$ s		Surwase et al. (2013)

kinetic parameters. When dissolution is combined with solution crystallization, the concentration-time profile becomes less steep. Therefore, the predicted concentration-time profiles vary for different amorphicity functions.

4.4. Validation of the proposed concept

4.4.1. Variation of amount of amorphous IND

Fig. 6 shows the predicted and measured supersaturation profiles for two different amounts (20 mg and 30 mg) of amorphous material and same amount of crystalline seeds (9 mg). A characteristic profile is observed, where the IND concentration initially increases fast before reaching a maximum value and decreasing afterwards. The profiles are asymmetric with respect to the maximum (i.e. spring is faster than parachute). For both predictions, the same kinetic parameters describing solution crystallization ($k_{t, C}$ and g_C) as well as the same amorphicity function ($\varphi_{\text{Greco, 7}}$) (see Table 2) were used. Dissolution kinetics were fitted individually due to the poor reproducibility encountered when different batches of the amorphous material are used. It can be seen that the supersaturation profiles differ. With higher amount of amorphous material, a higher maximum is reached at an earlier time compared to the profile for the lower amount of amorphous material. Notably, this is very well captured by the predicted profiles. This shows the validity of the proposed concept that the overall dynamics leading to the observed supersaturation profiles is a superposition of dissolution, crystal growth from solution, and solid-state transformation.

4.4.2. Variation of amount of crystalline IND seeds

Furthermore, the amount of crystalline seed material was varied. Fig. 7 shows a comparison of the supersaturation profiles obtained for two different amounts of crystalline seeds (6 mg and 9 mg) while the amount of amorphous material was kept constant at 20 mg. As expected, with lower amount of crystalline seeds, a higher peak concentration is observed, which is reached faster than with higher amount of crystalline seeds. The predictions with the $\varphi_{\text{Greco, 7}}$ amorphicity function yield good results in both cases and capture this effect very well.

4.4.3. Variation of solvent composition

To demonstrate transferability of the established concept, the solvent composition was changed. The concentration of ISO in the solvent was increased to 4 wt%. This was chosen so that the increase in ISO concentration was sufficient to significantly increase crystalline and
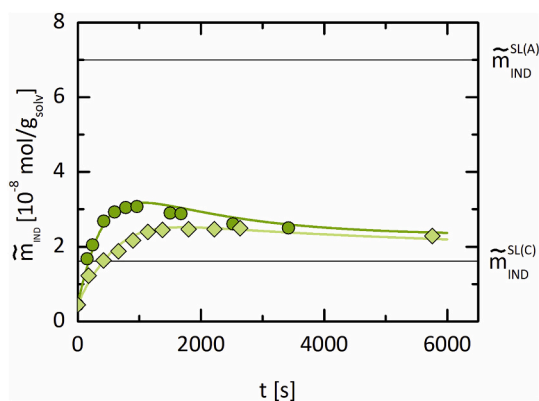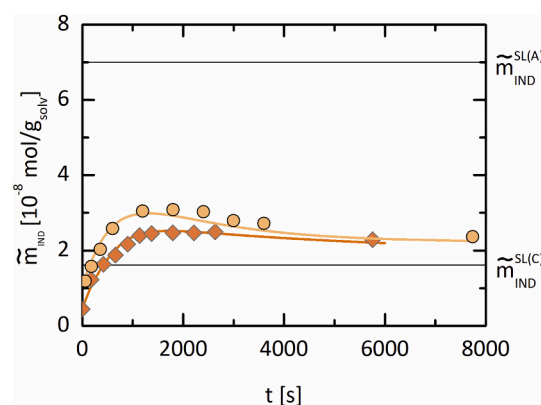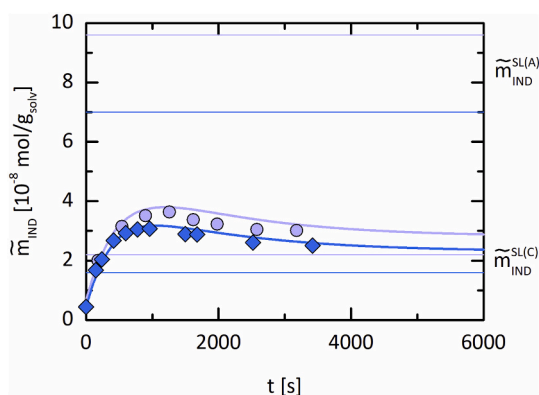
Fig. 7. Dissolution profiles of 20 mg amorphous IND in the presence of two different amount of crystalline IND seeds (diamonds: 9 mg, circles: 6 mg) in aqueous solution (0.4 wt% ISO) at 298.15 K and 460 rpm. Solid lines represent predictions with Eqs. (11) and (12) and amorphous-to-crystalline solid-state transformation is accounted for by the amorphicity function $\varphi_{\text{Greco, 7}}(t)$ derived from the intrisin-dissolution-rate data of Greco and Bogner at a flow rate of 7 mL/min.

amorphous solubility (factor 1.4) and at the same time not too drastic so that the amorphicity function would not change considerably. Separate experiments, where ISO was added dropwise onto amorphous material dispersed in water, showed fast surface crystallization on the amorphous particles. This occurred within one minute and suggests a drastic acceleration of the solid-state transformation kinetics. It is hypothesized that when amorphous particles experience high thermodynamic driving force for dissolution, a local built-up of supersaturation around the amorphous particle could lead to fast recrystallization directly on its surface (Surwase et al., 2013; Greco and Bogner, 2010). This effect would be enhanced at elevated ISO concentration due to its solubility-increasing effect. Alternatively, it could be hypothesized that fast dissolution creates intermolecular spaces that lead to higher molecular mobility at the surface. This allows molecules to rearrange and lead to a crystalline phase. In any case, this should manifest in a steeper amorphicity function. It was assumed that at the chosen concentration of 4 wt% ISO, the amorphicity function used before for the 0.4 wt% ISO systems (i.e. $\varphi_{\text{Greco, 7}}$) is still a sufficient representation of the true surface-transformation kinetics. Kinetic parameters can be found in Table 2. Due to higher amount of ISO, the obtained kinetic parameters vary slightly from those determined for the system with 0.4 wt% ISO.

Fig. 8 shows the comparison of dissolution profiles of 30 mg amorphous material in the presence of 9 mg crystalline seeds in aqueous solution containing 0.4 wt% and 4 wt% ISO. Both profiles show the characteristic supersaturation profile already described before. In the presence of higher concentrated ISO, a higher maximum is reached. This is a direct result from the increased amorphous and crystalline solubility, which accelerates dissolution and decelerates solution crystallization. The predictions capture this effect well.

4.4.4. Influence of PEG 400 on supersaturation profiles

As a final validation step, we tried to incorporate the influence of PEG 400 into the supersaturation profile. In earlier works, we learned that PEG in general only exhibits a thermodynamic effect on desupersaturation profiles by increasing the solubility of crystalline APIs. The solubility of crystalline IND in the presence of 0.5 wt% PEG 400 was measured. We assumed that the amorphous solubility was increased due to the presence of PEG by the same factor as the crystalline solubility. Amorphous particles showed agglomeration tendency in aqueous solution containing PEG 400. This manifested also in a less-steep initial dissolution profile. Therefore, separate kinetic parameters were determined for dissolution from a separate dissolution experiment in the absence of crystalline seeds. Consequently, the kinetic parameter k_t is

Fig. 6. Dissolution profiles of different amounts of amorphous IND (diamonds: 20 mg, circles: 30 mg (same as Fig. 2)) in the presence of 9 mg crystalline IND seeds in aqueous solution (0.4 wt% ISO) at 298.15 K and 460 rpm. Solid lines represent predictions with Eqs. (11) and (12) and amorphous-to-crystalline solid-state transformation is accounted for by the amorphicity function $\varphi_{\text{Greco, 7}}(t)$ derived from the intrisic-dissolution-rate data of Greco and Bogner at a flow rate of 7 mL/min.
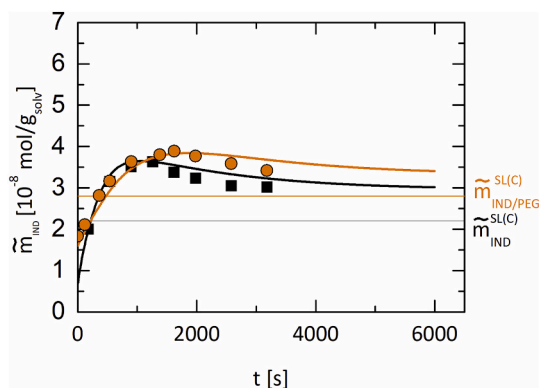
Fig. 8. Dissolution profiles of 30 mg amorphous IND in the presence of 9 mg crystalline IND seeds in aqueous solution with 0.4 wt% (diamonds) and 4 wt% (circles) of ISO at 298.15 and 460 rpm. Diamonds represent experimental data. Solid lines represent predictions with Eqs. (11) and (12) and amorphous-to-crystalline solid-state transformation is accounted for by the amorphicity function $\varphi_{\text{Greco},\,7}(t)$ derived from the intrisin-dissolution-rate data of Greco and Bogner at a flow rate of 7 mL/min.

significantly smaller than that for the polymer-free system (cp. Table 2). For crystallization, the same kinetic parameters were used as those in the polymer-free system. To be consistent with the established approach, also the same $\varphi_{\text{Greco},\,7}$ amorphicity function was used. Fig. 9 shows that the supersaturation profile, in particular the parachute effect, in the presence of PEG 400 is well predicted. The results strengthen our earlier finding that the influence of PEG can be captured fully by accounting for its solubility-increasing effect. Furthermore, PEG does not change the amorphicity function, which is consistent with this argumentation. As PEG binds preferentially to water due to its hydrophilicity (Price et al., 2019), it is reasonable that it does not change the surface transformation kinetics of amorphous APIs. The predictions capture this effect very nicely.

4.5. Interpretation of amorphicity function $\varphi(t)$

The results give a clear indication that surface-transformation kinetics is essential for understanding the supersaturation behavior of amorphous APIs in aqueous solution. Here, we want to discuss some properties of the amorphicity function, which we believe is a good representation of this kinetics. First, the amorphicity function seems to

Fig. 9. Dissolution profiles of 30 mg amorphous IND in the presence of 9 mg crystallline IND seeds in aqueous solution (4 wt% ISO) at 298.15 K and 460 rpm with (circles) and without (squares) 0.5 wt% PEG 400. Solid lines represent predictions with Eqs. (11) and (12) and amorphous-to-crystalline solid-state transformation is accounted for by the amorphicity function $\varphi_{\text{Greco},\,7}(t)$ derived from the intrisin-dissolution-rate data of Greco and Bogner at a flow rate of 7 mL/min.

only slightly depend on hydrodynamic conditions and is presumably independent of particle size. This manifests from the fact that the data of Greco and Bogner (2010), Surwase et al. (2013), as well as our own measurements lead to very similar amorphicity functions, although Greco and Bogner (2010) used smaller particles (150 μm) and different hydrodynamic conditions (Reynolds number of 2.4 and 34). Second, the solid-state transformation only occurs at regions exposed to dissolution medium. This was clearly visible from various experiments conducted in this work. Fig. 10 shows an amorphous NAP/PVP formulation before and after exposure to water for 1 min. It is obvious that only regions in contact with water show a crystallized surface after exposure. This formulation was chosen here, because it shows this effect in an accelerated time frame due to the fast crystallization tendency of NAP and the hygroscopicity of PVP.

Fig. 11 shows amorphous IND in water to which a drop of ISO was applied. Within 2 min, a crystalline layer was observed on top of the amorphous material. The excess ISO leads to fast dissolution and also accelerated the time frame for surface solid-state transformation.

Fig. 12 shows the amorphous IND disc recovered after the intrinsic-dissolution experiment performed in this work. The left hand side shows the surface not exposed to dissolution medium, while the right hand side shows the surface exposed to dissolution medium. Clearly, crystalline regions can be detected on its surface. From visual inspection one would roughly estimate 80% of the surface to have transformed. This would correspond to a amorphicity function value of 0.2, which is in general agreement with the amorphicity function extracted from the dissolution experiments (Fig. 4).

Third, the decrease of the amorphicity function (i.e. loss of amorphicity) is significantly faster than the increase in crystallinity reported by Andronis and Zografi obtained from sorption-induced crystallization at high relative humidity (up to 98% RH). This could either mean that these findings correspond to different mechanisms. Some reports in the literature hypothesize that the observed surface crystallization is a result of local supersaturation around the dissolving amorphous particles leading to recrystallization on the surface. Alternatively, this could be explained by the crystallinity observed in Andronis and Zografis sorption experiments. Depending on particle size and surface layer thickness, it could be plausible that only a few percent of crystallized mass fraction could correspond to significant surface coverage. This would in fact be detrimental, as long-term stability tests usually only consider crystallinity with respect to particle mass and not surface area.

Fourth, the amorphicity function employed throughout this work ($\varphi_{\text{Greco},\,7}(t)$) allowed for surprisingly accurate predictions of supersaturation profiles, when combined with dissolution and desupersaturation kinetics. Merely the tail section (after 2000 s) is overestimated slightly in most cases. This could be due to the amorphicity function being overestimated in this part. Alternatively, this overestimation could be caused by regarding the transformed regions as inert. While this assumption seems reasonable as long as dissolution is still considerably underway, it may be ill-advised at later times when dissolution has mostly ceased. Then, desupersaturation is likely to proceed also by growth at the transformed regions. If this was accounted for, the overestimation of the supersaturation profiles in the tail sections could potentially be remedied.

Last, the influence of polymeric excipients dissolved in the dissolution medium on the amorphicity function shall be briefly discussed. As expected, the supersaturation profiles in the presence of PEG can be well predicted with the same amorphicity function employed for the polymer-free systems. This demonstrates that PEG does not affect the kinetics of surface solid-state transformation represented by the amorphicity function. This is in line with our earlier findings where PEG did not alter molecular kinetics of crystal growth but rather acted thermodynamically as a solubilizer by increasing API equilibrium solubility. Due to its hydrophilicity, it interacts preferentially with water rather than the API. Other polymers like HPMC or PVP were shown to interact more strongly with the API. Various literature reports indicate that such
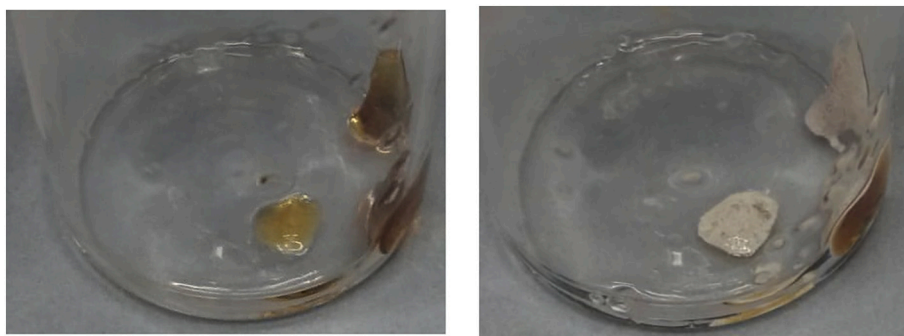
Fig. 10. Amorphous NAP/PVP (w_{NAP} = 0.4) formulation before (left hand side) and after (right hand side) exposure to water for 1 min.

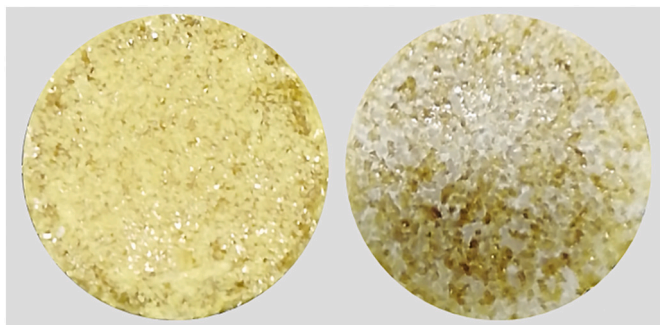**Fig. 11.** Amorphous IND exposed to water and a drop of ISO for 2 min.

Fig. 12. Disc of amorphous IND recovered after the intrinsic-dissolution experiments. The left hand side shows the surface not exposed to the dissolution medium. The right hand side shows the surface that was exposed to the dissolution medium.

polymers adsorb to API solid particles and inhibit nucleation and crystal growth kinetics. Alonzo et al. (2010) reported that in the presence of trace amounts of pre-dissolved HPMC and PVP, dissolution profiles of FEL and IND reached significantly higher solution concentrations than without the polymeric excipients. Thermodynamic effects can be ruled out due to the small concentration of the polymer. Aside from inhibiting solution crystallization kinetics, it can be hypothesized that the presence of the polymers also affects the kinetics of surface solid-state transformation. Specifically, it could inhibit this transformation so that the

resulting amorphicity function would be much less steep than the amorphicity function employed throughout this work. Mechanistically, it is fathomable that polymers in close proximity to the surface of dissolving amorphous solid reduce local supersaturation, thus inhibiting recrystallization at the surface and thereby solid-state transformation. Alternatively, it could be speculated that these polymers, by virtue of their hygroscopicity, bind water molecules at the surface of the amorphous solid that would otherwise be absorbed. In this way, surface mobility is not increased and reorientation of API molecules is hindered so that solid-state transformation is inhibited. In any case, it seems plausible that it is essential to quantify the influence of these polymers on solid-state transformation kinetics represented by the amorphicity function.

5. Conclusion

The present work is one of the first of its kind to integrate the relevant processes at play during dissolution of amorphous APIs in aqueous solution in an overall kinetic model that allows successful predictions of supersaturation profiles. Using IND as a model API, it was shown that by accounting for the kinetics of dissolution, solution crystallization and amorphous-to-crystalline solid-state transformation, very accurate predictions of the dissolution behavior were possible. The kinetics of solid-state transformation were quantified and embedded in an amorphicity function $\varphi(t)$. This function was derived consistently from different sets of experimental data and seems to be independent of the particle size of the amorphous material and hydrodynamic conditions.

The results highlight the importance of solid-state transformation on the overall supersaturation profile. Strikingly, solid-state transformation was found to occur on a considerably shorter time frame than that for vapor-sorption experiments at high relative humidity reported in the literature. This finding could prove to be invaluable in explaining the often-observed discrepancy between expected stability from long time storage experiments at elevated humidity and dissolution performance.

Declaration of Competing Interest

The authors declare that they have no known competing financial interests or personal relationships that could have appeared to influence the work reported in this paper.

Appendix A. Supplementarty data

References

Abbou Oucherif, K., Raina, S., Taylor, L.S., Litster, J.D., 2013. Quantitative analysis of the inhibitory effect of HPMC on felodipine crystallization kinetics using population balance modeling. Cryst. Eng. Comm. 15, 2197–2205.

Alonzo, D.E., Zhang, G.G.Z., Zhou, D., Gao, Y., Taylor, L.S., 2010. Understanding the behavior of amorphous pharmaceutical systems during dissolution. Pharm. Res. 27, 608–618.

Alonzo, D.E., Raina, S., Zhou, D., Gao, Y., Zhang, G.G.Z., Taylor, L.S., 2012. Characterizing the impact of hydroxypropylmethyl cellulose on the growth and nucleation kinetics of felodipine from supersaturated solutions. Cryst. Growth Des. 12, 1538–1547.

Andronis, V., Yoshioka, M., Zografi, G., 1997. Effects of sorbed water on the crystallization of indomethacin from the amorphous state. J. Pharm. Sci. 86, 346–351.

Cheng, H., Mao, L., Zhang, S., Lv, H., 2019. Impacts of polymeric additives on nucleation and crystal growth of indomethacin from supersaturated solutions. AAPS PharmSciTech 20, 193.

De Almeida, L.P., Simões, S., Brito, P., Portugal, A., Figueiredo, M., 1997. Modeling dissolution of sparingly soluble multisized powders. J. Pharm. Sci. 86, 726–732.

Greco, K., Bogner, R., 2010. Crystallization of amorphous indomethacin during dissolution: effect of processing and annealing. Mol. Pharm. 7, 1406–1418.

Guo, N., Hou, B., Wang, N., Xiao, Y., Huang, J., Guo, Y., Zong, S., Hao, H., 2018. In situ monitoring and modeling of the solution-mediated polymorphic transformation of rifampicin: from form II to form I. J. Pharm. Sci. 107, 344–352.

Guzmán, H.R., Tawa, M., Zhang, Z., Ratanabanangkoon, P., Shaw, P., Gardner, C.R., Chen, H., Moreau, J.-P., Almarsson, Ö., Remenar, J.F., 2007. Combined use of crystalline salt forms and precipitation inhibitors to improve oral absorption of celecoxib from solid oral formulations. J. Pharm. Sci. 96, 2686–2702.

Hancock, B.C., Parks, M., 2000. What is the true solubility advantage for amorphous pharmaceuticals? Pharm. Res. 17, 397–404.

Higuchi, T., 1961. Rate of release of medicaments from ointment bases containing drugs in suspension. J. Pharm. Sci. 50, 874–875.

Higuchi, T., 1963. Mechanism of sustained-action medication. Theoretical analysis of rate of release of solid drugs dispersed in solid matrices. J. Pharm. Sci. 52, 1145–1149.

Hirai, D., Iwao, Y., Kimura, S.-I., Noguchi, S., Itai, S., 2017. Mathematical model to analyze the dissolution behavior of metastable crystals or amorphous drug accompanied with a solid-liquid interface reaction. Int. J. Pharm. 522, 58–65.

Ji, Y., Paus, R., Prudic, A., Lübbert, C., Sadowski, G., 2015. A novel approach for analyzing the dissolution mechanism of solid dispersions. Pharm. Res. 32, 2559–2578.

Korsmeyer, R.W., Gurny, R., Doelker, E., Buri, P., Peppas, N.A., 1983. Mechanisms of solute release from porous hydrophilic polymers. Int. J. Pharm. 15, 25–35.

Langham, Z.A., Booth, J., Hughes, L.P., Reynolds, G.K., Wren, S.A.C., 2012. Mechanistic insights into the dissolution of spray-dried amorphous solid dispersions. J. Pharm. Sci. 101, 2798–2810.

Lindfors, L., Skantze, P., Skantze, U., Westergren, J., Olsson, U., 2007. Amorphous drug nanosuspensions. 3. Particle dissolution and crystal growth. Langmuir 23, 9866–9874.

Moseson, D.E., Parker, A.S., Beaudoin, S.P., Taylor, L.S., 2020. Amorphous solid dispersions containing residual crystallinity: influence of seed properties and polymer adsorption on dissolution performance. Eur. J. Pharm. Sci. 146, 105276.

Murdande, S.B., Pikal, M.J., Shanker, R.M., Bogner, R.H., 2010. Solubility advantage of amorphous pharmaceuticals: I. A thermodynamic analysis. J. Pharm. Sci. 99, 1254–1264.

Murdande, S.B., Pikal, M.J., Shanker, R.M., Bogner, R.H., 2011. Aqueous solubility of crystalline and amorphous drugs: challenges in measurement. Pharm. Dev. Technol. 16, 187–200.

Nogami, H., Nagai, T., Yotsuyanagi, T., 1969. Dissolution phenomena of organic medicinals involving simultaneous phase changes. Chem. Pharm. Bull. 17, 499–509.

Novakovic, D., Peltonen, L., Isomäki, A., Fraser-Miller, S.J., Nielsen, L.H., Laaksonen, T., Strachan, C.J., 2020. Surface stabilization and dissolution rate improvement of amorphous compacts with thin polymer coatings: can we have it all? Mol. Pharm. 17, 1248–1260.

Noyes, A.A., Whitney, W.R., 1897. The rate of solution of solid substances in their own solutions. J. Am. Chem. Soc. 19, 930–934.

Patel, D.D., Anderson, B.D., 2014. Effect of precipitation inhibitors on indomethacin supersaturation maintenance: mechanisms and modeling. Mol. Pharm. 11, 1489–1499.

Patel, D.D., Anderson, B.D., 2015. Adsorption of polyvinylpyrrolidone and its impact on maintenance of aqueous supersaturation of indomethacin via crystal growth inhibition. J. Pharm. Sci. 104, 2923–2933.

Paus, R., Ji, Y., Braak, F., Sadowski, G., 2015a. Dissolution of crystalline pharmaceuticals: experimental investigation and thermodynamic modeling. Ind. Eng. Chem. Res. 54, 731–742.

Paus, R., Ji, Y., Vahle, L., Sadowski, G., 2015b. Predicting the solubility advantage of amorphous pharmaceuticals: a novel thermodynamic approach. Mol. Pharm. 12, 2823–2833.

Price, D.J., Nair, A., Kuentz, M., Dressman, J., Saal, C., 2019. Calculation of drug-polymer mixing enthalpy as a new screening method of precipitation inhibitors for supersaturating pharmaceutical formulations. Eur. J. Pharm. Sci. 132, 142–156.

Randolph, A.D., Larson, M.A. (Eds.), 1971. Theory of Particulate Processes. Academic Press.

Savolainen, M., Kogermann, K., Heinz, A., Aaltonen, J., Peltonen, L., Strachan, C., Yliruusi, J., 2009. Better understanding of dissolution behaviour of amorphous drugs by in situ solid-state analysis using Raman spectroscopy. Eur. J. Pharm. Biopharm. 71, 71–79.

Schneider, R., Taspinar, L., Ji, Y., Sadowski, G., 2020. The influence of polymeric excipients on desupersaturation profiles of active pharmaceutical ingredients. 1: polyethylene glycol. Int. J. Pharm. 582, 119317.

Schram, C.J., Smyth, R.J., Taylor, L.S., Beaudoin, S.P., 2016. Understanding crystal growth kinetics in the absence and presence of a polymer using a rotating disk apparatus. Cryst. Growth Des. 16, 2640–2645.

Štukelj, J., Svanbäck, S., Agopov, M., Löbmann, K., Strachan, C.J., Rades, T., Yliruusi, J., 2019. Direct measurement of amorphous solubility. Anal. Chem. 91, 7411–7417.

Surwase, S.A., Boetker, J.P., Saville, D., Boyd, B.J., Gordon, K.C., Peltonen, L., Strachan, C.J., 2013. Indomethacin: new polymorphs of an old drug. Mol. Pharm. 10, 4472–4480.

Wu, T., Yu, L., 2006. Surface crystallization of indomethacin below Tg. Pharm. Res. 23, 2350–2355.